Published in *Computers in Biology and Medicine, 2019, vol. 115, 103505* which should be cited to refer to this work
DOI: 10.1016/j.compbiomed.2019.103505

An Automated Segmentation Framework for Nasal Computational Fluid Dynamics Analysis in Computed Tomography

Robin Huang[1], Anthony Nedanoski[2,3], David F. Fletcher[4], Narinder Singh[6], Jerome Schmid[5], Paul M. Young[3], Nicholas Stow[3], Lei Bi[1], Daniela Traini[3], Eugene Wong[6], Craig L. Phillips[7], Ronald R. Grunstein[7], Jinman Kim[1]

[1] School of Computer Science, University of Sydney, Australia
[2] School of Mechanical and Aerospace Engineering, University of Sydney, Australia
[3]Discipline of Pharmacology, Faculty of Medicine and Heath and Woolcock Institute of Medical Research, University of Sydney, Australia
[4] School of Chemical and Molecular Engineering, University of Sydney, Australia
[5] Geneva School of Health Sciences, HES-SO University of Applied Sciences and Arts Western Switzerland, Switzerland
[6]Department of Otolaryngology, Westmead Hospital and University of Sydney, Australia
[7]CIRUS, Sleep and Circadian Group, Woolcock Institute of Medical Research and Faculty of Medicine and Health, University of Sydney

Corresponding author:
Name: Robin Huang
Email: robin.huang@sydney.edu.au

ABSTRACT

The use of computational fluid dynamics (CFD) to model and predict surgical outcomes in the nasal cavity is becoming increasingly popular. Despite a number of well-known nasal segmentation methods being available, there is currently a lack of an automated, CFD targeted segmentation framework to reliably compute accurate patient-specific nasal models. This paper demonstrates the potential of a robust nasal cavity segmentation framework to automatically segment and produce nasal models for CFD. The framework was evaluated on a clinical dataset of 30 head Computer Tomography (CT) scans, and the outputs of the segmented nasal models were further compared with ground truth models in CFD simulations on pressure drop and particle deposition efficiency. The developed framework achieved a segmentation accuracy of 90.9 DSC, and an average distance error of 0.3 mm. Preliminary CFD simulations revealed similar outcomes between using ground truth and segmented models. Additional analysis still needs to be conducted to verify the accuracy of using segmented models for CFD purposes.

Keywords–nasal cavity; image segmentation; computational fluid dynamics; computed tomography

1. Introduction

The nasal cavity's primary role is to provide humidified, warmed, filtered air before entering the lungs. Secondary functions include facilitating olfaction, along with ventilation of the paranasal sinuses. To achieve these specific but varied functions, the nasal cavity has a complex anatomical structure. Physiological and anatomical conditions in the nasal cavities can result in significant sequelae in the lower respiratory system. In addition, nasal airway disorders can also disturb other homeostatic systems, such as sleep and cardiovascular health [1, 2]. Each year, more than 340,000 patients in North America undergo surgery to correct nasal airway obstruction [2]. However, up to 37% of patients report unsatisfactory or no improvement after such surgery [3-5]. One of the key reasons for this high failure rate is the lack of objective methods to predict surgical outcomes [5].

In recent years, computational fluid dynamics (CFD) has been proposed as a potential tool for modelling and predicting surgical outcomes using patient-specific nasal models [5-7]. Through the use of computer-assisted numerical analysis and simulations, it is possible for CFD to accurately model and derive key metrics, such as nasal resistance, airflow rate, wall shear stress and heat fluxes. While previous studies have demonstrated the validity and effectiveness of CFD in modelling the nasal airway [6, 8-10], the process of patient-specific model creation remains time and labour intensive. There is a critical need for an efficient, reliable and automated framework to generate patient-specific nasal models to conduct CFD.

CFD outcomes are heavily reliant on the accuracy of the patient-specific model used. In order to produce an anatomically accurate model of a patient's nasal cavity, high quality segmentation is essential. However, due to the complexity of the nasal cavity anatomy and its connectivity to other airway components of similar intensity values, such as the paranasal sinuses, it is often difficult to differentiate and segment just the nasal cavity alone, without performing manual delineation [11]. Figure 1 exemplifies the close proximity of the paranasal sinuses to the nasal cavity and highlights the connectivity between the two regions. The majority of existing nasal segmentation methods have either included nearby airway components as part of the segmentation [12-18], or require some form of manual intervention in order to derive results [17-22].

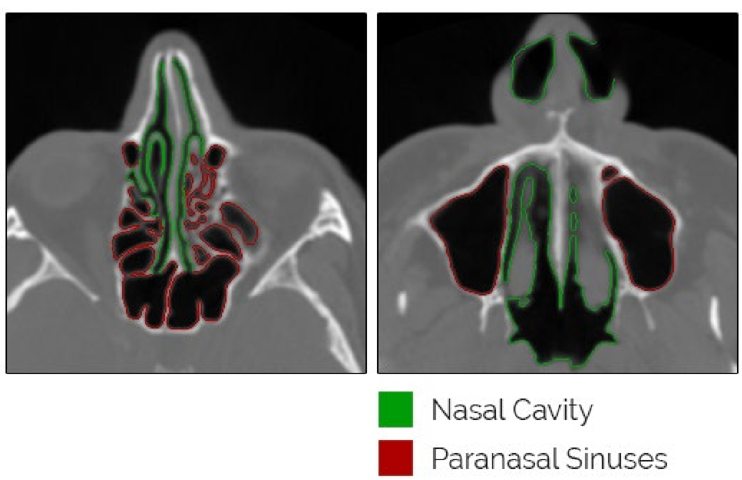

Figure 1: Examples illustrating the issues involved in segmenting the nasal cavity due to the lack of boundary distinction to other airway regions.

In the work of Bui et al. [12], a multi-step level-set segmentation procedure was utilised to automatically segment the nasal cavity and the surrounding paranasal sinuses from cone-beam computed tomography (CBCT). Whereas Last et al. [13] utilised a level-set based deformable model to segment the nasal cavity and paranasal sinuses. Other works have used more traditional methods such as thresholding [15, 16] or region growing [14, 17, 18], where they rely on the similar voxel intensity range, as well as the interconnectivity of the upper airways to make the segmentation. While these methods were effective at segmenting airway regions within the human body, they were not able to identify individual components nor separate them based on anatomical information. Currently, it is difficult to accurately label the boundaries without manual intervention. This is evident among studies that focused on segmenting just the nasal cavity itself, such as in the works of Kimura et al. [20] and Alsufyani et al. [22] where thresholding was used to segment the upper airway, and large amounts of manual delineation was required in order to separate the nasal cavity from the rest of the airway regions.

Keustermans et al. [21] made use of an active shape model (ASM) to semi-automatically segment the nasal cavity. An ASM is a landmark based statistical shape model (SSM) segmentation method which makes use of anatomical knowledge derived from a set of training data to segment a particular organ or structure [23, 24]. By modelling the shape variability of the nasal cavity beforehand, they were able to use that information to significantly reduce the amount of manual intervention required during segmentation when compared with other literature works, demonstrating the powerful capability of an SSM.

In order to achieve a faster and more efficient way of segmenting the nasal cavity, an SSM is essential for determining the boundaries between the nasal cavity and other airway components. Although [21] made use of a landmark based SSM for segmentation, it is limited due to the reliance on point correspondence for shape model representation. As ASMs require every training shape to be constructed with the same number of points (landmarks) that corresponds, it is difficult to include and model features or shapes that exist outside the norm. For our goal of establishing patient-specific nasal models for CFD, where a large majority could likely to be those with diseased or obstructed airways, we require a method which can reliably segment all kinds of cases. Level-set approaches, which are based on evolving contours do not require point correspondence and can still incorporate statistical and anatomical knowledge as shape priors into its energy formulation [25, 26]. Although there are known weaknesses for level-set methods during the segmentation process such as becoming trapped inside a local minimum, these weaknesses can be avoid when combined with other segmentation methods [27]. As region-based segmentation methods like region growing have been shown to be effective at segmenting airway regions, combining shape priors from a level-set SSM with a more advanced region-based method would be the most logical approach for nasal cavity segmentation.

In this study, we demonstrate the efficiency of an automated segmentation framework at optimizing the nasal model creation process for CFD. Compared with our previous work [11], our proposed framework makes the following distinctions: (i) the initialization process through the use of superpixels has been improved [28], in combination with a multi-atlas for seed derivation; and (ii) the framework has been optimized to reduce the number of manual steps needed for the CFD, by incorporating post-smoothing and cleaning algorithms, as well as automating the process of pressure inlet and outlet creation using spatial and anatomical information. The framework was evaluated on a clinical dataset of 30 head CT scans, and the outputs of the nasal models generated using the segmentation framework were further tested against ground truth models in CFD simulations. Statistical tests were performed to assess the outcome of the segmented models against ground truth models for pressure drop and particle deposition.

2. Methods

Our algorithm requires the use of a statistical shape model (SSM) which needs to be constructed prior to segmentation. The segmentation framework can be divided into three main sections: initialization, segmentation, and post-processing.

2.1 SSM Construction

SSM construction was based on the method of Leventon et al. [25], where a mean offset matrix of the nasal training data, denoted as $\{x_1 - \bar{x}, x_2 - \bar{x}, \ldots, x_n - \bar{x}\}$ is constructed, with x_1 to x_n being the signed distance representations of the training shapes and $\bar{x}$ being the mean denoted as $\bar{x} = \frac{1}{n}\sum_{i=1}^{n} x_i$. The resulting eigenvector $\boldsymbol{U}$ and eigenvalues obtained from the singular value decomposition (SVD) of the mean offset matrix holds the decomposed features of the nasal cavity shape. An estimate of a novel nasal shape s_{est}, can be represented by k principal components in a k-dimensional vector of coefficients, α:

$$S_{est} = U_k\alpha + \bar{x}. \tag{1}$$

For the selection of the training data, we assigned a weight w to each nasal shape t, where $w = \frac{|P \cap t|}{|P|+|t|-|P \cap t|}$. Nasal shapes that scored below the third quartile were removed from the training dataset.

2.2 Initialization

An atlas consists of a Computed Tomography (CT) image and a corresponding ground truth segmentation. Affine and Bspline registration using Elastix [29] was first applied to align n atlas CT images to the input target image. The transformation parameters of the registration were then applied on the atlas segmentations to warp them to the same reference frame as the target image. A probabilistic multi-atlas A was constructed as the average of the registered segmentations $\{G_1, G_2, \ldots, G_n\}$ over the total number of atlases n, denoted as $A = \frac{1}{n}\sum_{j=1}^{n} G_j$.

Thresholding was applied on the input image to extract the position of the airway voxels. By overlaying A on top of the thresholded image T, an estimate P of the nasal cavity was obtained from the union of the thresholded image and the atlas, defined as: $P = A \cup T$. The input image was further cropped in order to better localize the nasal cavity and to reduce the computation time. Smaller and detached airway regions captured by P were removed to ensure accurate seed derivation. We applied the SLIC superpixel [28] algorithm on the cropped image. Foreground seeds are derived from the cluster centres of the superpixels on the largest airway region that lay within P at a slice by slice level. Background seeds were derived from the cluster centres of tissue regions and airway regions a distance σ away from P, with σ being a numerical parameter specified during initialization. Once the required seeds were derived and an estimate of the nasal cavity P was obtained, the shape priors to capture the statistical variances of the nasal cavity were constructed.

2.3 Segmentation

The constructed SSM was embedded in a graph-based segmentation framework and an image was formulated as a graph $G = (V, E)$, where each vertex $v \in V$ corresponds to an image voxel and each edge $e \in E$ connects two vertices in V. We utilized the base method of random walk (RW) and formulated the Dirichlet energy as $E_{rw} = z^T Lz$, where L is the Laplacian matrix defined in [30] and denotes the pairwise affinities among the vertices in V, and $z \in R^{|V|\times 2}$ is a labeling vector indicating voxel foreground (background) probabilities. In our nasal cavity segmentation problem, we defined a new energy term which holds the captured shape variances from the nasal SSM to the labeling vector of image voxels. The labeling vector can be optimized by solving a graph Dirichlet problem to produce the final probabilistic labeling. The proposed energy term was defined as:

$$E_{\ priors} = (z - (U_k\alpha + \bar{x}_{prob}))^{\mathrm{T}}(z - (U_k\alpha + \bar{x}_{prob})) \quad (2)$$

where $\bar{x}_{prob} = \frac{1}{1+\exp(\bar{x})}$ and $z = \begin{bmatrix} z_M \\ z_N \end{bmatrix}$, where z_M denotes the predefined labels, i.e. foreground and background seeds, and z_N denotes other labels. Given the definition of E_{priors}, the complete energy function is formulated as $E_{total} = E_{rw} + E_{priors}$.

An estimation of the nasal cavity shape was obtained by minimizing the proposed functional $E_{total}(z_N, \alpha)$, iteratively, with respect to each of its variables z_N and α. Starting from $\alpha = 0$, the mean shape was initialized over the input image. Since E_{total} is convex, we differentiate E_{total} with respect to z_N and find the critical point yielding:

$$z_N = (L_N + I)^{-1}(2(U_k\alpha + \bar{x}_{prob}) - B^{\mathrm{T}} z_M) \quad (3)$$

where I is an identity matrix, L is the Laplacian matrix of the image and B is the matrix partitioned from L which correlates the labeled set to the unlabeled set. Secondly, we use the updated z_N to differentiate E_{total} once more with respect to α, which yields the following:

$$\alpha = (U_k^{\mathrm{T}} U_k)^{-1} U_k^{\mathrm{T}} (z_N - \bar{x}). \quad (4)$$

In order to reduce the amount of over-segmentation while still maintaining the effects of our shape priors, the output of E_{total} was constrained to remain within the boundaries of the nasal airway by computing a probability of the estimated foreground voxels and removing those that were located in the tissue regions based on their intensity value at each step of the differential iteration.

2.4 Post-Processing and CFD preparation

Post-processing smoothing and cleaning were required in order to prepare the output segmentations for CFD modelling. An adaptive smoothing algorithm was applied to smooth the edges that contained rough and jagged surfaces. A connected regions tool was applied to filter out displaced segmentation noise to ensure a single solid object was outputted to STL which could then be meshed for flow simulation. The entrances and exit of the nasal model were automatically detected using spatial and anatomical information, and automatically extended by the algorithm in order to clearly establish the inlet and outlet locations needed in the CFD model. The final segmentation output was converted into STL ready to be meshed for CFD simulation.

2.5 CFD Model Creation

ANSYS Fluent Meshing (version 17.0) was used to create the mesh. The inflow and outflow regions of the nasal geometry were first separated from the wall region. Once imported, a wrapping algorithm was applied with minimum and maximum surface mesh sizes of 0.1 mm and 2.5 mm, respectively. These parameter values were selected empirically after a dimensioned rectangular prism was introduced as a body of influence which acted as a secondary sizing control limiting the size of surface mesh to a maximum of 0.1 mm in regions of the nasal cavity that were separated by narrow gaps. Once the volumetric region was computed it was automatically meshed using polyhedral elements growing according to the local size field of the region. Inflation was applied at all walls with the Fluent Meshing default algorithm, which uses a first aspect ratio of 10, last aspect ratio of 4.8, growth rate of 1.2 and is set to generate five layers at the walls. Node locations were then automatically adjusted by systematically reducing the threshold for the maximum skewness to approximately 0.6. The final nasal mesh was imported directly into the ANSYS Fluent solver ready for simulation.

3. Materials and Evaluation Setup

3.1 Materials

Our dataset which consisted of 30 de-identified head CT scans was acquired from the Department of Radiology at the Royal Prince Alfred hospital (Camperdown, NSW, Australia), following approval from the Sydney Local Health District Ethics Committee. The subjects of the 30 CT scans were all males of Caucasian descent over the age of 40 with different nasal or sinus related complaints. The scans were acquired using a GE Lightspeed-16 CT Scanner using Helical CT imaging protocols with an average exposure time of 707 ms. The resulting images maintained a resolution of 220 by 220 mm (512×512 voxels) and a voxel depth of 1.25 mm. The ground truth data were semi-automatically segmented using Geodesic Image Segmentation [31] by an experienced operator under the guidance of a nasal surgeon. Each segmentation took approximately 15 minutes to complete. The segmented data were further re-examined by a clinical doctor with expertise in CT scan interpretation. The resulting ground truth segmentations were used in our algorithm as both training data for the level-set SSM and for the construction of the probabilistic atlas.

3.2 Segmentation Evaluation Setup

The leave-one-out cross validation was performed on 30 CT images (30 folds), where 29 ground truth labels were used each time for the creation of the PA and SSM. The initialization parameter was set to $\sigma = 5$, which was derived empirically based on experiment validations. We compared our framework with the locally constrained statistical shape model (LC-SSM) [11] and evaluated our method on both segmentation accuracy and time. We conducted our experiment on a Windows 8.1 64-bit Desktop PC with i5-3470 3.2 GHz processor and 16 GB DDR3 RAM.

The following metrics were used for the evaluation of segmentation results: (i) dice similarity coefficient (DSC) calculated as the overlap between the two volumes according to: $DSC = \frac{2\,|X \cap Y|}{|X|+|Y|}$, where X is the segmentation label and Y is the ground truth label; (ii) average symmetric surface distance (ASSD in mm); (iii) average symmetric root mean square surface distance (ASRSD in mm); (iv) maximum surface distance (MSD in mm); and (v) volumetric overlap error (VOE in %). Further details on the evaluation metrics can be found in Heimann et al. [32].

3.3 CFD Evaluation Setup

Of the 30 nasal segmentation outputs, the best and worst segmentation case based on DSC along with 8 additional segmentation outputs were selected and CFD simulation constructed using ANSYS Fluent solver (version 17.0). The outcomes of the CFD simulation using the nasal segmentation models were directly compared against the corresponding ground truth nasal models. Two-tailed paired t test was utilized to assess the mean difference between using segmented and ground truth nasal models, and a p value less than 0.05 was considered statistically significant.

We based the parameter setting for CFD on Engelhardt et al. [33] which models airflow and particle deposition in the nasal cavity and presents calculated Reynolds (Re) numbers for various flow rates. For the breathing rate of 30 L/min a Re > 3000 was calculated, indicating turbulent flow. A flow rate of 30 L/min was selected to replicate fast nasal inhalation as would practically occur with administration of therapeutic nasal sprays. As such, the flow was modelled using the realizable *k*-*ε* turbulence model and a target mass flow rate of 6.13×10^{-4} kg/s (30 L/min) set at the pressure outlet. The total pressure at the inlet was set to 0 Pa (gauge). The coupled solver was used with convergence achieved when the locally scaled residuals fell below 10^{-4}, which typically required 200 iterations.

Once the simulation was converged, Lagrangian particle tracking with a turbulent dispersion model was applied. The particle diameter size distribution was described using the Rosin-Rammler distribution, with the distribution parameters determined from laser diffraction experimental data obtained by analyzing water plumes from a spray bottle using a Malvern Spraytec®. The minimum and maximum diameters were set to 0.12 µm and 1000 µm, respectively, with a mean diameter of 85.8 µm and a spread parameter of 1.92. After the flow had converged, water droplets were injected from each inlet and the simulation completed when all the particles had either escaped from the outlet or collided with the rigid walls of the nasal cavity, which was set to trap particles upon contact.

4. Results

4.1 Segmentation

Table 1 presents the segmentation results of our framework compared with the LC-SSM, evaluated based on the metrics described in section 3.2. Our method achieved an averaged Dice Similarity Coefficient (DSC) of 90.9%, an averaged Surface Distance error of 0.3 mm, and an averaged Volumetric Overlap Error (VOE) of 16.6%. Figure 2 contains the DSC for each individual segmentation case, with case 23 achieving the best result (97.1%) and case 9 the worst (85.1%).

Segmentation Accuracy	*DSC*	*ASSD*	*ASRSD*	*MSD*	*VOE*
Our method	$\mathbf{90.9 \pm 2.9}$	$\mathbf{0.30 \pm 0.}1$	$\mathbf{0.86 \pm 0.3}$	$\mathbf{7.5 \pm 1.7}$	$\mathbf{16.6 \pm 4.8}$
LC-SSM	90.4 ± 3.1	0.31 ± 0.1	0.86 ± 0.3	7.8 ± 2.0	17.2 ± 5.4

Table 1: Comparative evaluation of our segmentation framework with the LC-SSM.

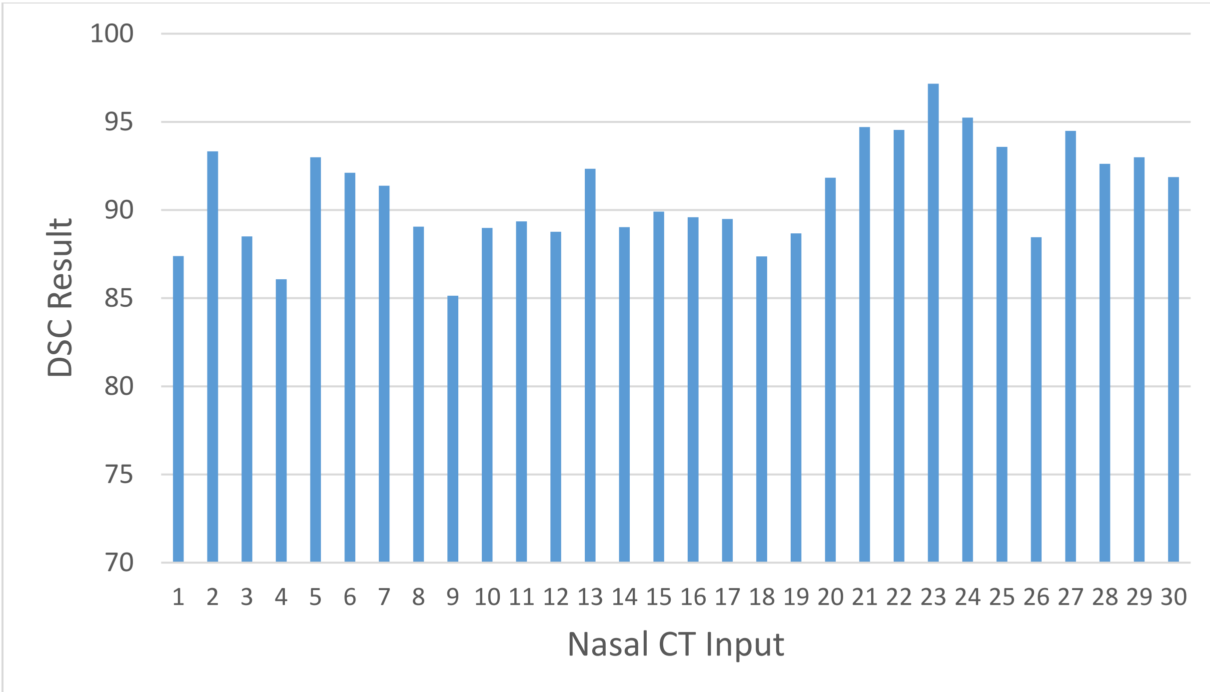

Figure 2: DSC results of each nasal segmentation

Table 2 illustrates the average segmentation speed of our framework. The initialization process took on average 328 seconds to complete, where most of the time was spent on image registration. An average of 11.5 seconds was required for the segmentation process to complete. When combining initialization, segmentation, and post-processing, the total average time was 339.6 seconds.

Segmentation Speed	*Initialization*	*Segmentation*	*Post-processing*	*Total*
Our method	$328s \pm 3.1s$	$11.5s \pm 1.8s$	$<1s \pm 0.05s$	$339.6s \pm 2.2s$

Table 2: Speed of our segmentation framework

4.2 CFD

Case 23 and case 9 were selected as the best and worse segmentation cases based on the DSC result. Cases 6, 10, 12, 15, 17, 18, 21, 25 were selected based on their combined average score (90.6 DSC) which was the nearest to the reported mean DSC average. Figure 3 presents the pressure drop (Pa) for each nasal segmentation case compared against their respective ground truth model. The pressure drops ranged from

3.5 Pa (lowest) to 29 Pa (highest), and the results were relatively consistent between the segmented and ground truth models with the exceptions of cases 9 and 18 where the differences in pressure drop were 1.6 Pa (25%) and 2.2 Pa (35%), respectively.

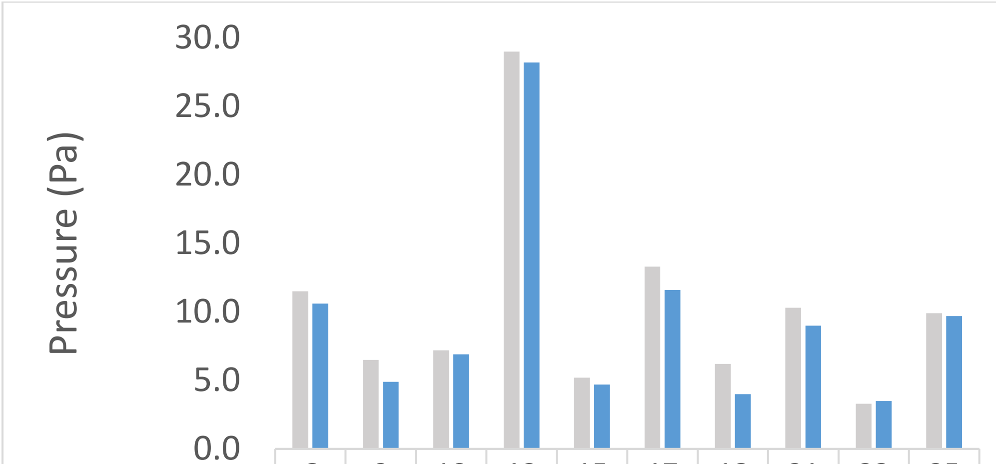

	6	9	10	12	15	17	18	21	23	25
Ground Truth	11.5	6.5	7.2	29.0	5.2	13.3	6.2	10.3	3.3	9.9
Segmented	10.6	4.9	6.9	28.2	4.7	11.6	4.0	9.0	3.5	9.7

Figure 3: A summary of the pressure drop calculated for the different cases. Results shown in grey are for the ground truth models whereas those in blue are for the segmented models.

Figure 4 presents the particle deposition efficiency across the 10 pairs of nasal models calculated as the percentage of the input mass flow of particles that were trapped on the walls. The percentage trapped ranged from 90% to 97%. Overall, there were very few differences found between the ground truth and segmented models. Even for cases that demonstrated greater variation in airflow between the ground truth and segmented models (case 9 and 18), the particle deposition remained consistent.

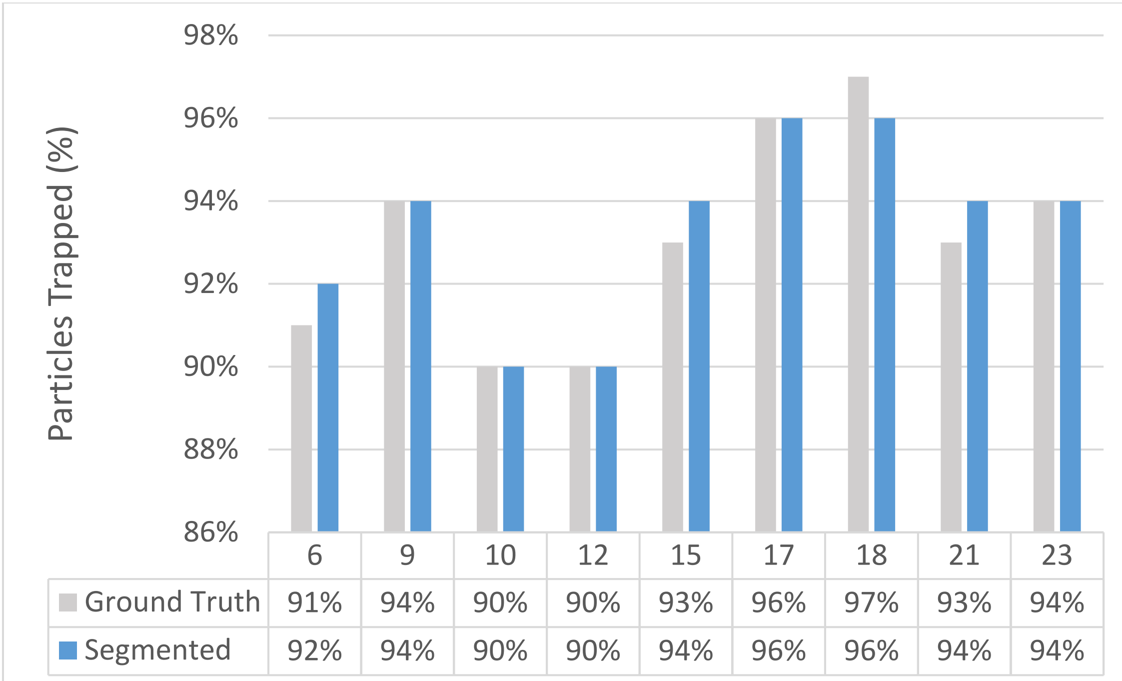

Figure 4: The percentage of particle deposited on the walls of the nasal geometry for each case: ground truth model (grey) and segmented models (blue).

When examining individual cases, both the ground truth and segmented models revealed similar pressure distributions across all 10 nasal pairs. Overall, the region comprising of the nasal vestibule and the nasal valve were observed to contain the highest pressure drop and velocity magnitude. Figure 5 illustrates the wall pressure and the streamline plots of airflow for case 10, where regions of higher pressure in the left nostril, as well as in the middle to upper region of the nasal cavities were observed. The outer (inferior turbinate) regions displayed less pressure drop when compared with the others, indicating that most of the airflow was centred primarily on the middle turbinate region and further disperses to the upper regions.

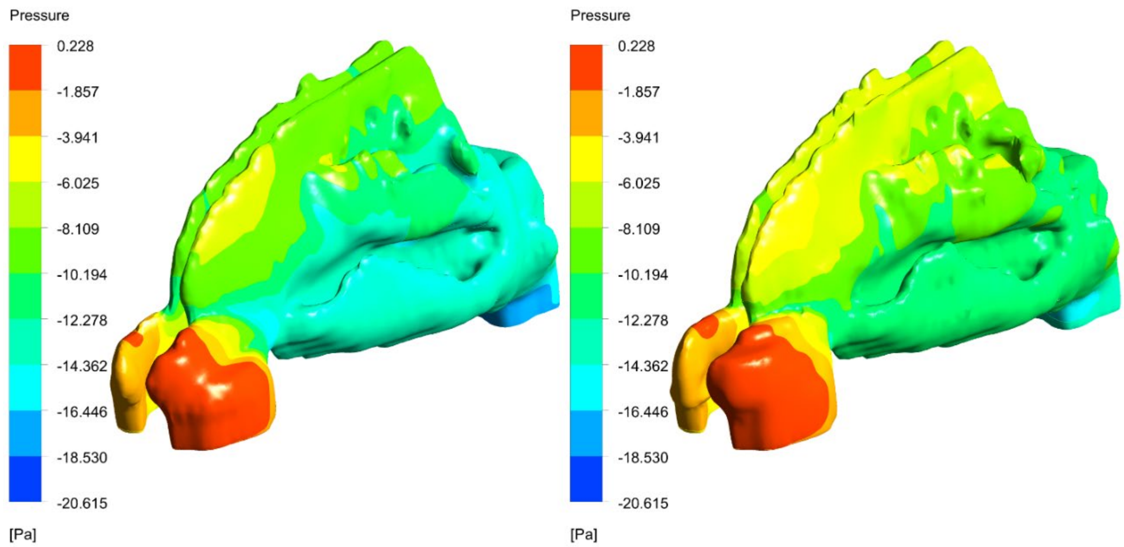

Figure 5a. Wall pressure plots of case 10 with the ground truth model (left) and segmented model (right) indicating the overall change in pressure across the mode from approximately –21 Pa to 0.2 Pa.

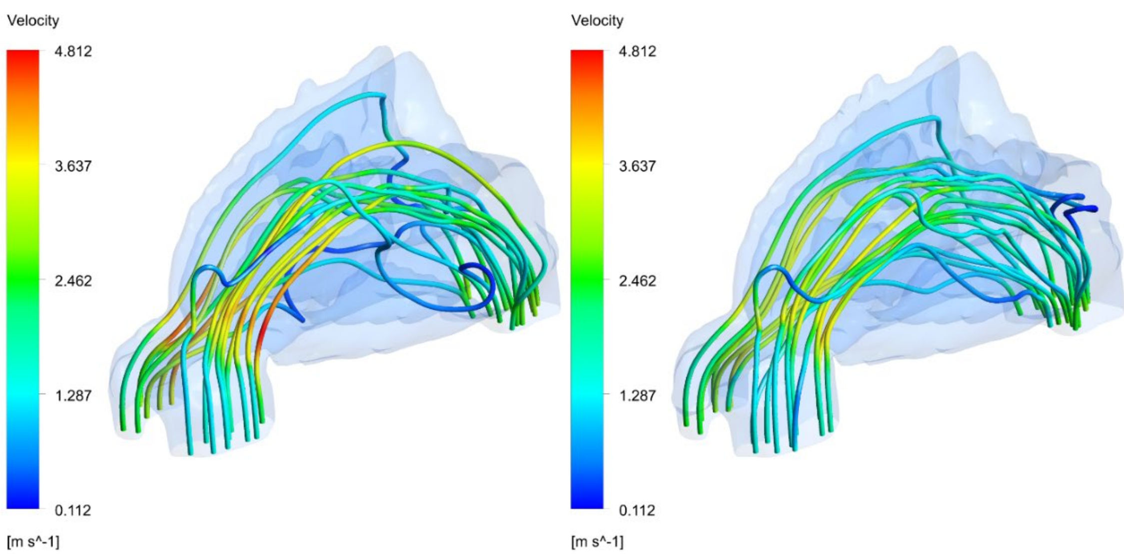

Figure 5b: Streamline plots, coloured by velocity magnitude, of case 10 originating from the inlets for the ground truth (left) and the segmented model (right) colored by velocity magnitude.

When looking at the airflow velocities, the middle regions experienced a higher velocity (3.6 m/s) on average when compared with the upper regions (1.29 m/s). Figure 6 illustrates the velocity magnitudes shown in cross sectional view, where higher velocities were observed in the regions close to the centre of each passage, with the highest velocity magnitude (4.7 m/s) occurring in the region adjacent and superior to the inferior turbinate of the ground truth model. While the segmented model revealed a similar albeit slightly lower velocity magnitude (4.2 m/s). Despite the similar flow behavior exhibited between the ground truth and segmented models, ground truth models were observed on average to have higher velocity magnitudes than their counterpart.

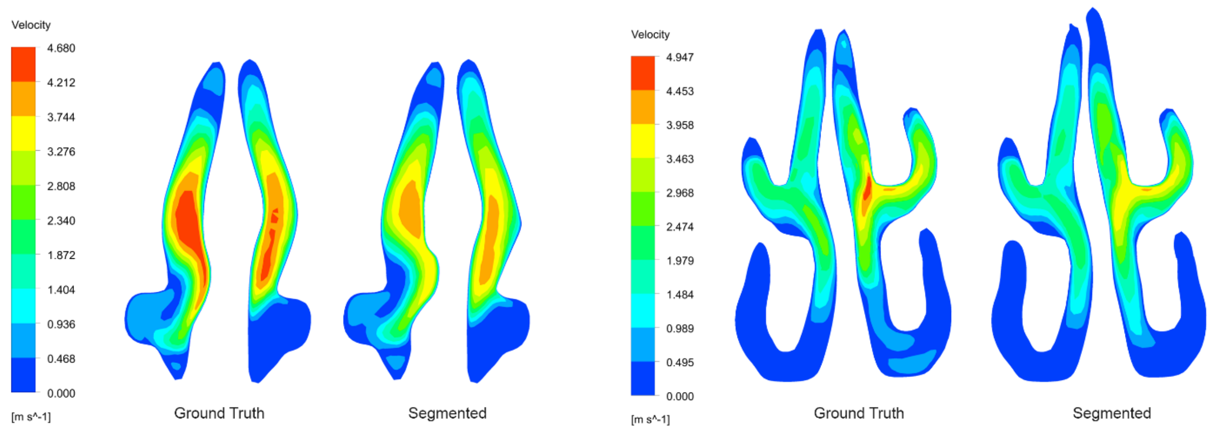

Figure 6: Examples of cross sectional view comparison on the local velocity magnitude. The left example shows the cross section at 20mm from the front of the model, and the right example at 40mm from the front of the model.

Table 3 presents the overall CFD outcomes between using ground truth and segmented nasal models. No significant difference was observed between ground truth and segmented nasal models for pressure drop (p = 0.061) and particle deposition (p = 0.279)

Overall Outcomes	*Ground Truth*	*Segmented*	*p value*
Pressure Drop (Pa)	10.2	9.3	0.061
Particle Deposition (%)	93	93	0.278

Table 3: Mean pressure drop (Pa) and percentage of particles trapped for the ground truth and segmented nasal models. Two-tailed paired t test was conducted to derive the p values.

5. Discussion

Overall, our framework was able to automatically segment the nasal cavity from CT images at a relatively fast and efficient pace. When compared with our previous method, we were able to improve the segmentation accuracy due to the changes made to the initialization process. As a large portion of the nasal cavity consists of thin and narrow pathways that are often located in very close proximity to each other, where sometimes the distance is as thin as two voxels apart, it is especially important to be able to clearly define the foreground and background seeds during initialization. With the use of superpixel clusters, we were able to minimize over-extension and ensure a more robust selection of foreground seeds.

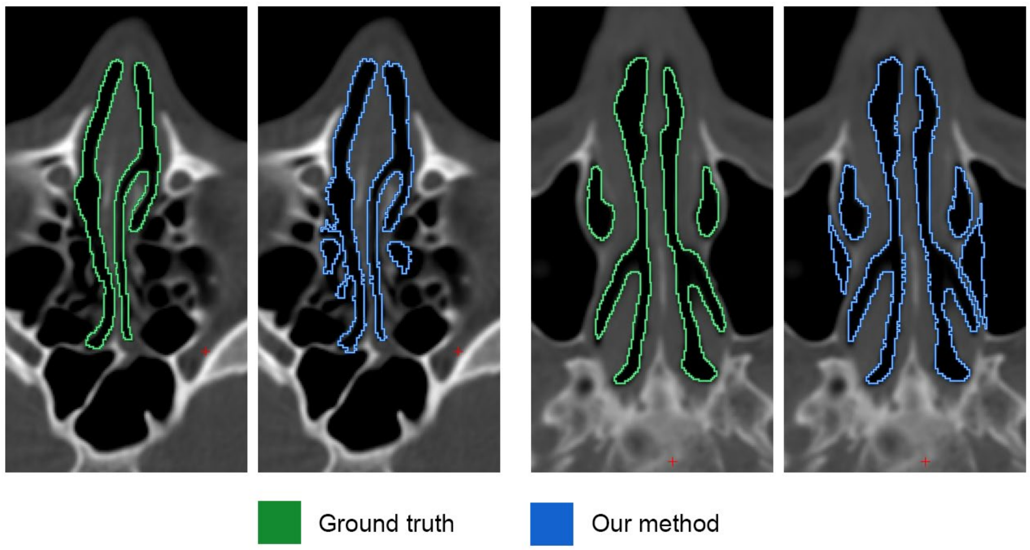

Figure 7: Examples of some of the worst segmentation errors with ground truth labels for comparison. The left side (case 1) depicts a commonly encountered error of leakage into ethmoid sinuses, while the right side (case 9) depicts a rare over segmentation error that expanded into the maxillary sinuses.

When comparing our results with ground truth segmentation, we noticed that despite having leveraged the use of a level set SSM, it was still difficult for our method to accurately label some of the boundaries, especially at the regions surrounding the superior meatus. Based on CT observations, these regions of the nasal cavity are often in very close proximity to the ethmoid sinuses. Entrances connecting the two airway components are not fixed, which makes it difficult for an algorithm to correctly judge when to cut the segmentation. The majority of our results have experienced some form of leakage at this region of the nasal cavity. The left side of figure 7 shows an example of this problem where parts of the segmentation leaks into the ethmoid sinuses. The example shown on the right side highlights the worst case of over-segmentation where due to similar issues, would sometimes cause leakage into the maxillary sinuses. However, even for our worst case, the size of the leakage was kept relatively contained due to the effect of our SSM.

As the primary objective of our study was centred on creating patient-specific nasal models to conduct CFD simulations, it was important for our framework to be able to reduce as many of the steps needed prior to conducting the simulations. Prior to adding the post-processing method component to our framework, we analysed the key differences between our segmented results and the ground truth models. The first apparent difference discovered was in the cell count of the mesh. As a result of the sensitivity of the segmentation process, a large majority of the segmented models had artefactual regions in their morphology, which do not appear in the ground truth models. Most of these artefacts appear to represent paranasal sinus cells, particularly ethmoid cells above the middle turbinate, such as in case 12. In many cases, these cells are connected to the main body of the nasal cavity by narrow channels which when meshed produce large cell counts because many small-sized cells are required to resolve these regions. During manual segmentation, these cells are typically excluded from segmentation. We were able to reduce this issue by adding an extra post-processing cleaning step where algorithms such as 6-way connected regions were applied on the segmentation outputs in order to remove those that were in the neighbourhood of almost touching or clipping the central superior nasal airway.

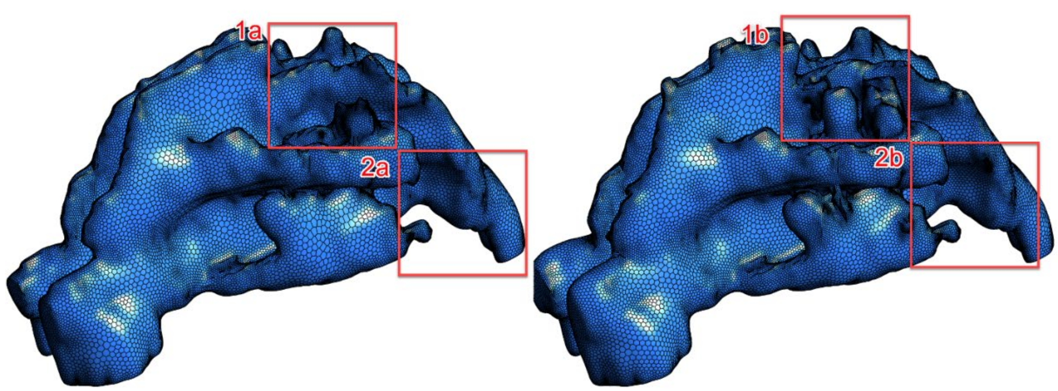

Figure 8: The geometry of the nasal cavity for case 12. The model on the left is the ground truth model and that on the right is the segmented model. Region 1a and 1b demonstrate the ethmoid sinus region on the model and region 2a and 2b demonstrate lateral enlargement of the posterior end of the inferior turbinate restricting airflow to the nasopharynx.

Nevertheless, it remained difficult to fully remove these artefact cells as it would risk exclusion of the narrow central superior nasal airway that passes immediately between the ethmoid region and the septum. Looking at case 12 in particular (Figure 8), it was observed that it contained a number of such artefacts. Additionally, region 2a and 2b revealed a disconnection between the airflow beneath and around the inferior turbinate and the nasopharynx which although is consistent in both the segmented and ground truth models, it is not commonly observed in other nasal pairs. When examining the CT image for case 12 in closer detail, we noticed lateral enlargement of the posterior end of the inferior turbinate in both nasal cavities, restricting airflow to the nasopharynx and causing both the ground truth and segmented models to be disconnected in that particular section. In addition, significant medial obstruction in the right nasal cavity of the patient was observed, resulting in marked reduction in airflow. These sites of obstruction were the primary reason for the higher pressure drop and increased particle retention which remained consistent in both segmented and ground truth models. In all other models, the largest pressure drops were noted in the vestibule and nasal valve area, as is typically seen in the nasal CFD literature [34, 35]. If all models were chosen to represent clear noses, case 12 would be omitted.

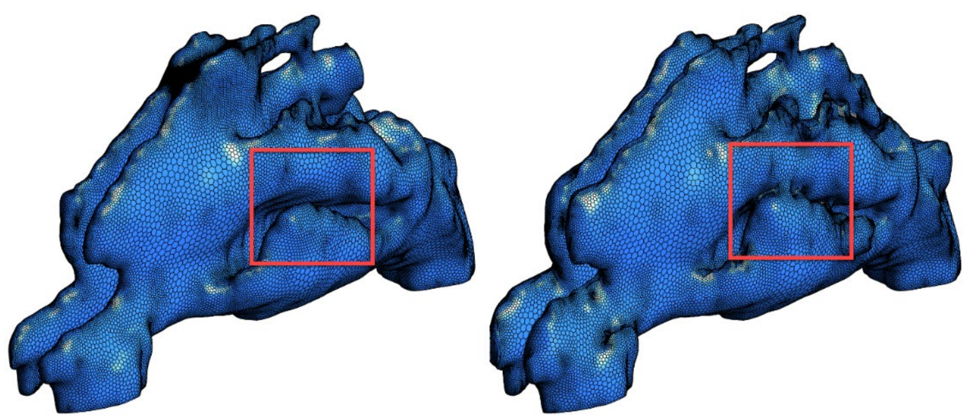

Figure 9: The nasal cavity geometry for case 21. The model on the left is the ground truth model and that on the right is the segmented model. The region highlighted by the red square shows a narrow connection formed between the air passage beneath and above the inferior turbinate in the segmented model.

In addition to incorporating ethmoid cells within the segmented model, another artefact was identified, whereby the segmented model would rarely connect adjacent passages which would normally be separated by very thin tissue. For example, in case 21, in the segmented model, a narrow connection was formed between the air passage beneath and above the inferior turbinate (Figure 9) that does not appear in the ground truth model. Although the artefact captured in this example appears small and creates little impact on the overall nasal segmentation accuracy, its effect on the internal structure remains significant. Such artefacts create small holes within the geometry allowing flow to pass through, creating pressure and velocity differences between the ground truth and segmented models. It is an important issue to address when designing segmentation algorithms with the intent of performing CFD simulations, as artefacts such as these would alter the expected physical air flow patterns contrary to the actual nasal structure of the patients from which the CT scans are obtained.

5.1 Other work

While the majority of our discussions have been on the accuracy and limitations of our proposed framework, it is important to also discuss and compare with other related works in general. In the work presented by Last et al. [13], they made use of a parametric level-set based deformable model to segment the region of interest (ROI) containing the nasal cavity and paranasal sinuses. Different to other studies, their intended segmentation target was not just the airway passages but also included the bones and tissues situated within the nasal region, as the aim of their segmentation was to identify the critical structures in robot assisted functional endoscopic sinus surgery. The base component of their method was the same as our segmentation framework where an SSM was constructed from training data. However, the segmentation approach they employed was a geodesic contour based method [25] and they segmented the CT image one 2D slice at a time, breaking down the targeted 3D structure into individual components. Such an approach is capable of achieving high performance for 2D objects but inherently has a higher probability of sharp local jumps in the combined 3D result.

Keustermans et al. [21] employed an ASM for their nasal cavity segmentation. Different to level-set methods, ASM makes use of landmarks for SSM construction. This approach was highly popular due to the memory efficiency of using a fewer number of features called “landmarks” to represent a modelled structure, whereas for level-set SSMs every voxel has a corresponding SDM representation. Both approaches have their strength and weaknesses. For landmark approaches, it is difficult to model complex shapes with high degrees of variation such as the nasal cavity. While for level-set approaches, larger numbers of eigen-modes are required due to the intrinsic nature of modelling the variations on the space of embedded contours. Nevertheless, the flexibility offered from level-set SSMs are higher as they have higher degrees of freedom and be combined with a number of other methods for segmentation to overcome some of its weaknesses.

6. Conclusions

This paper presents an efficient automated framework for the 3D segmentation of the nasal cavity, optimized for CFD modelling. Our framework achieved a segmentation accuracy of 90.9 DSC and an average distance error of 0.3 mm. The nasal models generated from our framework were further evaluated by calculating flow and droplet impact behaviour using the CFD model ANSYS Fluent in comparison with the models constructed from ground truth segmentation. Similar outcomes were observed for pressure drop and particle deposition efficiency between the two groups. We note that the proposed method still shows some differences that affect the flow locally and we are currently working on methods to detect these using the CFD data.

Conflict of Interest

Robin Huang, Anthony Nedanoski, David Fletcher, Jerome Schmid, Paul Young, Nicholas Stow, Lei Bi, Daniela Traini, Eugene Wong, Craig Phillips, Ron Grunstein, Narinder Singh, and Jinman Kim declare that they have no conflict of interest.

Acknowledgement

This research was partly funded by the Australian Research Council.

References

[1] N. Mygind and R. Dahl, "Anatomy, physiology and function of the nasal cavities in health and disease," *Advanced drug delivery reviews,* vol. 29, no. 1-2, pp. 3-12, 1998.

[2] N. Bhattacharyya, "Ambulatory sinus and nasal surgery in the United States: demographics and perioperative outcomes," *The Laryngoscope,* vol. 120, no. 3, pp. 635-638, 2010.

[3] H. Dommerby, O. R. Rasmussen, and J. Rosborg, "Long-term results of septoplastic operations," *ORL,* vol. 47, no. 3, pp. 151-157, 1985.

[4] A. Singh, N. Patel, G. Kenyon, and G. Donaldson, "Is there objective evidence that septal surgery improves nasal airflow?," *The Journal of Laryngology & Otology,* vol. 120, no. 11, pp. 916-920, 2006.

[5] A. AT Borojeni, D. O. Frank‐Ito, J. S. Kimbell, J. S. Rhee, and G. J. Garcia, "Creation of an idealized nasopharynx geometry for accurate computational fluid dynamics simulations of nasal airflow in patient‐specific models lacking the nasopharynx anatomy," *International journal for numerical methods in biomedical engineering,* vol. 33, no. 5, p. e2825, 2017.

[6] S. K. Kim, Y. Na, J.-I. Kim, and S.-K. Chung, "Patient specific CFD models of nasal airflow: overview of methods and challenges," *Journal of biomechanics,* vol. 46, no. 2, pp. 299-306, 2013.

[7] J. Cisonni, A. D. Lucey, A. J. King, S. M. S. Islam, R. Lewis, and M. S. Goonewardene, "Numerical simulation of pharyngeal airflow applied to obstructive sleep apnea: effect of the nasal cavity in anatomically accurate airway models," *Medical & biological engineering & computing,* pp. 1-11, 2015.

[8] G. J. de Moraes Garcia, N. A. Bailie, D. A. Martins, and J. S. Kimbell, "Atrophic rhinitis: a CFD study of air conditioning in the nasal cavity," *Journal of applied physiology,* 2007.

[9] P. W. Longest and S. Vinchurkar, "Validating CFD predictions of respiratory aerosol deposition: effects of upstream transition and turbulence," *Journal of biomechanics,* vol. 40, no. 2, pp. 305-316, 2007.

[10] J. Wen, K. Inthavong, J. Tu, and S. Wang, "Numerical simulations for detailed airflow dynamics in a human nasal cavity," *Respiratory physiology & neurobiology,* vol. 161, no. 2, pp. 125-135, 2008.

[11] R. Huang *et al.*, "A Locally Constrained Statistical Shape Model for Robust Nasal Cavity Segmentation in Computed Tomography," in *International Symposium on Biomedical Imaging: From Nano to Macro (ISBI)*, 2016, pp. 1-4: IEEE.

[12] N. L. Bui, S. H. Ong, and K. W. C. Foong, "Automatic segmentation of the nasal cavity and paranasal sinuses from cone-beam CT images," *International journal of computer assisted radiology and surgery,* vol. 10, no. 8, pp. 1269-1277, 2015.

[13] C. Last, S. Winkelbach, F. M. Wahl, K. W. Eichhorn, and F. Bootz, "A model-based approach to the segmentation of nasal cavity and paranasal sinus boundaries," in *Pattern Recognition*: Springer, 2010, pp. 333-342.

[14] K. Tingelhoff *et al.*, "Comparison between manual and semi-automatic segmentation of nasal cavity and paranasal sinuses from CT images," in *2007 29th Annual International Conference of the IEEE Engineering in Medicine and Biology Society*, 2007, pp. 5505-5508: IEEE.

[15] A. S. El, H. El, J. M. Palomo, and D. A. Baur, "A 3-dimensional airway analysis of an obstructive sleep apnea surgical correction with cone beam computed tomography," *Journal of Oral and Maxillofacial Surgery,* vol. 69, no. 9, pp. 2424-2436, 2011.

[16] T. Iwasaki *et al.*, "Evaluation of upper airway obstruction in Class II children with fluid-mechanical simulation," *American Journal of Orthodontics and Dentofacial Orthopedics,* vol. 139, no. 2, pp. e135-e145, 2011.

[17] A. Seo, S. Chung, J. Lee, J.-I. Kim, and H. Kim, "Semiautomatic segmentation of nasal airway based on collaborative environment," in *Ubiquitous Virtual Reality (ISUVR), 2010 International Symposium on*, 2010, pp. 56-59: IEEE.

[18] P. Dastidar, T. Heinonen, J. Numminen, M. Rautiainen, and E. Laasonen, "Semi-automatic segmentation of computed tomographic images in volumetric estimation of nasal airway," *European archives of oto-rhino-laryngology,* vol. 256, no. 4, pp. 192-198, 1999.
[19] K. Tingelhoff *et al.*, "Comparison between manual and semi-automatic segmentation of nasal cavity and paranasal sinuses from CT images," in *Engineering in Medicine and Biology Society, 2007. EMBS 2007. 29th Annual International Conference of the IEEE*, 2007, pp. 5505-5508: IEEE.
[20] S. Kimura *et al.*, "Voxel-based modeling of airflow in the human nasal cavity," *Computer methods in biomechanics and biomedical engineering,* pp. 1-9, 2019.
[21] W. Keustermans, T. Huysmans, B. Schmelzer, J. Sijbers, and J. J. Dirckx, "Matlab® toolbox for semi-automatic segmentation of the human nasal cavity based on active shape modeling," *Computers in biology and medicine,* vol. 105, pp. 27-38, 2019.
[22] N. A. Alsufyani *et al.*, "New algorithm for semiautomatic segmentation of nasal cavity and pharyngeal airway in comparison with manual segmentation using cone-beam computed tomography," *American Journal of Orthodontics and Dentofacial Orthopedics,* vol. 150, no. 4, pp. 703-712, 2016.
[23] T. F. Cootes, C. J. Taylor, D. H. Cooper, and J. Graham, "Active shape models-their training and application," *Computer vision and image understanding,* vol. 61, no. 1, pp. 38-59, 1995.
[24] T. Heimann and H.-P. Meinzer, "Statistical shape models for 3D medical image segmentation: a review," *Medical image analysis,* vol. 13, no. 4, pp. 543-563, 2009.
[25] M. E. Leventon, W. E. L. Grimson, and O. Faugeras, "Statistical shape influence in geodesic active contours," in *Computer Vision and Pattern Recognition, 2000. Proceedings. IEEE Conference on*, 2000, vol. 1, pp. 316-323: IEEE.
[26] A. Wimmer, G. Soza, and J. Hornegger, "A generic probabilistic active shape model for organ segmentation," in *International Conference on Medical Image Computing and Computer-Assisted Intervention*, 2009, pp. 26-33: Springer.
[27] D. Cremers, M. Rousson, and R. Deriche, "A review of statistical approaches to level set segmentation: integrating color, texture, motion and shape," *International journal of computer vision,* vol. 72, no. 2, pp. 195-215, 2007.
[28] R. Achanta, A. Shaji, K. Smith, A. Lucchi, P. Fua, and S. Süsstrunk, "SLIC superpixels compared to state-of-the-art superpixel methods," *IEEE transactions on pattern analysis and machine intelligence,* vol. 34, no. 11, pp. 2274-2282, 2012.
[29] S. Klein, M. Staring, K. Murphy, M. A. Viergever, and J. P. Pluim, "Elastix: a toolbox for intensity-based medical image registration," *Medical Imaging, IEEE Transactions on,* vol. 29, no. 1, pp. 196-205, 2010.
[30] L. Grady, "Random walks for image segmentation," *Pattern Analysis and Machine Intelligence, IEEE Transactions on,* vol. 28, no. 11, pp. 1768-1783, 2006.
[31] A. Criminisi, T. Sharp, and A. Blake, "Geos: Geodesic image segmentation," in *Computer Vision–ECCV 2008*: Springer, 2008, pp. 99-112.
[32] T. Heimann *et al.*, "Comparison and evaluation of methods for liver segmentation from CT datasets," *Medical Imaging, IEEE Transactions on,* vol. 28, no. 8, pp. 1251-1265, 2009.
[33] L. Engelhardt, M. Röhm, C. Mavoungou, K. Schindowski, A. Schafmeister, and U. Simon, "First steps to develop and validate a CFPD model in order to support the design of nose-to-brain delivered biopharmaceuticals," *Pharmaceutical research,* vol. 33, no. 6, pp. 1337-1350, 2016.
[34] C. Croce *et al.*, "In vitro experiments and numerical simulations of airflow in realistic nasal airway geometry," *Annals of biomedical engineering,* vol. 34, no. 6, pp. 997-1007, 2006.
[35] D. Doorly, D. Taylor, and R. Schroter, "Mechanics of airflow in the human nasal airways," *Respiratory physiology & neurobiology,* vol. 163, no. 1-3, pp. 100-110, 2008.